Comparative EBSD Analysis of Fracture Behavior in Powder Metallurgy High-Speed Steel

Firouzi, Ahmad; Yazdani, Sasan; Petrov, Roumen H.; Shakerifard, Behnam; Khan, M. D.F.

DOI
10.1007/s11837-025-07538-1

Publication date
2025

Document Version
Final published version

Published in
JOM

Citation (APA)
Firouzi, A., Yazdani, S., Petrov, R. H., Shakerifard, B., & Khan, M. D. F. (2025). Comparative EBSD Analysis of Fracture Behavior in Powder Metallurgy High-Speed Steel. *JOM*, *77*(9), 6957-6970. https://doi.org/10.1007/s11837-025-07538-1

JOM
https://doi.org/10.1007/s11837-025-07538-1

TECHNICAL ARTICLE

Comparative EBSD Analysis of Fracture Behavior in Powder Metallurgy High-Speed Steel

AHMAD FIROUZI,[1] SASAN YAZDANI ,[1,5] ROUMEN H. PETROV,[2,3] BEHNAM SHAKERIFARD,[3] and MD. F KHAN[4]

1.—Faculty of Materials Engineering, Sahand University of Technology, Tabriz 53318/17634, Iran. 2.—Department of Electromechanical Systems & Metal Engineering, Ghent University, 9000 Ghent, Belgium. 3.—Department of Materials Science and Engineering, Delft University of Technology, 2628 CD Delft, Netherlands. 4.—Department of Mechanical Engineering, College of Engineering, King Faisal University, 31982 Al-Hofuf, Saudi Arabia. 5.—e-mail: Yazdani@sut.ac.ir

This study compares the fracture toughness of high-speed steel produced by powder metallurgy and subjected to different heat treatments to obtain either martensitic or bainitic/martensitic microstructures. The heat-treatment process involved austenitization at 1150 °C, followed by either martempering or austempering at 235 °C, and final tempering. Microstructural analysis was performed using electron backscatter diffraction (EBSD), field-emission scanning electron microscopy (FESEM), and X-ray diffraction (XRD). Fracture toughness was evaluated using circumferential notched tensile (CNT) specimens. The results showed that austempered CNT samples exhibited significantly higher fracture toughness compared to martempered ones, indicating improved resistance to crack propagation. Microstructural characterization revealed distinct differences: the austempered samples featured bainitic laths, retained austenite blocks, and martensite plates, whereas the martempered sample contained martensite plates and austenite islands. However, small differences in prior austenite grain size, lath thickness, and dislocation density were insufficient to fully account for the enhanced toughness in the austempered sample. Further analysis indicated that the increased fraction of high-angle grain boundaries and higher kernel average misorientation (KAM) in the austempered sample acted as effective barriers to crack propagation. Additionally, a greater volume fraction of nano-sized carbides contributed to a more pronounced strengthening effect, further enhancing fracture toughness.

List of Symbols

A_{C1}	The temperature at which austenite begins to form during heating
AM	Austenite/martensite islands
BL	Bainitic lath
B/M	Bainitic/Martensite
Bs	The starting temperature of the bainitic transformation
b	Burger's vector
CI	Confidence index
d	Grain size
D	Diameter of hard particles
D_c	Mean diameter size of undissolved carbides
d_0	Specimen diameter
d_n	Notch diameter
F	Fracture load
f	Fraction of hard particles
f_c	Surface area fraction of undissolved carbides
FC	Fine carbides
G	Shear modulus
GB	Grain boundary
GND	Geometrically necessary dislocation density
HAGB	High angle grain boundary
IPF	Inverse pole figure
IQ	Image quality
KAM	Kernal average misorientation

(Received January 30, 2025; accepted May 27, 2025)

Published online: 10 July 2025

Kc	Fracture toughness
kV	Kilovolts
LAGB	Low angle grain boundary
M	Taylor factor
MP	Martensite plates
M_S	The starting temperature of the martensitic transformation
ML	Martensitic lath
MCC	Circumscribed circle diameter in prior austenite grain
MIC	Largest inscribed circle in prior austenite grain
SSD	Statistically stored dislocation
UC	Undissolved carbides
β_{hkl}:	Full-width at half-maximum
σ_d	Strengthening contribution attributed to dislocations
σ_f	Fracture strength
σ_p	Strengthening contribution associated with precipitation carbides
σ_{ss}	Strengthening contribution attributed to solid solution
σ_T	Increase in yield strength
σ_Y	Strengthening contribution attributed to grain size
ε	Microstrain
θ	Bragg angle
ρ_{GND}	Dislocation density of GND
ρ_{SSD}	Dislocation density of SSD

INTRODUCTION

High-speed steels (HSS) are a class of tool steels widely used in cutting and machining applications due to their exceptional combination of high hardness, wear resistance, and hot hardness; that is, the ability to maintain hardness and mechanical strength at elevated temperatures.[1–4] These properties are primarily achieved through a carefully controlled heat-treatment process, which typically involves austenitizing, quenching to form martensite, and multiple tempering cycles. The tempering process is critical for reducing retained austenite, which is inherently high in HSS due to its complex alloy composition, and for enhancing the material's hardness and wear resistance. Typically, two or three tempering cycles at 500–600 °C are employed, reducing the retained austenite content from approximately 30% to 2–4% and increasing the hardness to 62–64 HRC.[5] Despite these favorable properties, HSS tools are prone to failure under severe operating conditions, particularly at cutting edges or regions subjected to high tensile stresses.[6,7] Such failures often result in costly downtime and tool replacement, underscoring the need to improve the fracture toughness of HSS. One promising approach to enhancing fracture toughness in HSS is through microstructural modification, particularly by incorporating bainitic microstructures into the steel matrix. Bainitic transformation is known to refine grain structure, increase high-angle grain boundaries (HAGBs), and improve crack propagation resistance, all of which are beneficial for enhancing fracture toughness.[8–10]

Several studies have explored the influence of bainitic microstructures on steel toughness.[11–16] For example, Chakraborty et al.[17] demonstrated that ultrafine bainitic sheaves interspersed with thin martensitic plates significantly improve fracture toughness in high-carbon low-alloy steels. Luo et al.[16] emphasized that bainite/martensite lath structures' toughness is strongly influenced by packet and block size, with a finer substructure improving toughness. Wang et al.[18] found that tempering bainite/martensite (B/M) duplex structures in M50 steel results in finer ferrite packets and increased precipitation of nanoscale carbides compared to fully martensitic structures, leading to improved impact toughness. The morphology of bainite also plays a crucial role in toughness enhancement. Lath-like upper bainite, consisting of thin parallel ferrite laths, has been reported to provide superior impact toughness compared to granular bainite due to its refined and ductile nature.[19] The presence of film-like retained austenite between bainitic ferrite laths further enhances the combination of toughness, ductility, and strength.[20] Furthermore, reducing the size of bainitic units has been shown to enhance crack resistance by increasing HAGBs, thereby improving low-temperature fracture toughness.[8,9]

While previous studies have extensively explored the bainitic transformation in lower-alloy steels, high-speed steels have received comparatively less attention in this context. Most research on HSS fracture behavior has focused on martensitic microstructures, with limited studies investigating the potential advantages of bainitic structures. Given the high carbide content and complex alloying of HSS, the formation and stabilization of bainitic microstructures pose unique challenges that remain largely unexplored. This gap in knowledge is critical, as an optimized bainitic microstructure could offer improved fracture toughness without significantly compromising hardness.

This study aims to address this research gap by analyzing the bainitic and martensitic microstructures of PM ASP2030, an alloy consisting of W-Mo-Cr-Co-Si-V, which is widely used for cutting tool applications due to its superior properties. These properties are primarily attributed to its production method (powder metallurgy) and chemical composition. Advanced characterization techniques such as electron backscatter diffraction (EBSD) analysis are employed in this study. The silicon present in the steel composition influences bainitic transformation by promoting a finer bainitic structure[21] and stabilizing austenite,[22] which in turn facilitates a more homogeneous distribution of carbides during tempering, ultimately enhancing the steel's toughness.

Based on these considerations, this study hypothesizes that the martempering process will yield a fully martensitic microstructure, optimizing hardness and wear resistance but potentially increasing brittleness due to the high internal stresses. In contrast, the austempering process is expected to produce a bainitic microstructure, which enhances fracture toughness while maintaining sufficient hardness. By investigating these two heat-treatment processes, this study seeks to provide a deeper understanding of the microstructure–property relationships in PM ASP2030, with a particular focus on optimizing mechanical performance for cutting tool applications.

EXPERIMENTAL

Material and Sample Preparation

The raw material used in this study was a 20-mm-diameter round bar of Erasteel™ PM ASP2030, processed via powder metallurgy (PM) followed by hot isostatic pressing. The chemical composition, determined using a Spectrolab M8™ spark emission analyzer, is provided in Table I. The bar was cut into specimens of 15-mm and 125-mm lengths for subsequent microstructural and mechanical analyses. Circumferential notch tensile (CNT) specimens, machined according to the DIN 7168 standard, were used for fracture toughness testing (Fig. 1).[4,23]

Heat Treatment

The selection of martempering and austempering heat treatment cycles was guided by the continuous cooling transformation (CCT) diagram of PM ASP2030 steel. The key transformation temperatures, martensite start (Ms) and bainite start (Bs), were calculated using:[24,25]

$$\mathrm{Bs}(^\circ\mathrm{C}) = 630 - 45(\mathrm{Mn}) - 40(\mathrm{V}) - 35(\mathrm{Si}) - 30(\mathrm{Cr}) - 25(\mathrm{Mo}) - 20(\mathrm{Ni}) - 15(\mathrm{W}) \quad (1)$$

$$\mathrm{Ms}(^\circ\mathrm{C}) = 539 - 423(\mathrm{C}) - 30.4(\mathrm{Mn}) - 12.1(\mathrm{Cr}) - 17.7(\mathrm{Ni}) - 7.5(\mathrm{Mo}) \quad (2)$$

All the samples underwent a controlled preheating cycle before austenitization to minimize thermal gradients and reduce the risk of cracking.[26] The preheating steps were performed at 550 °C and 850 °C for 30 and 15 min, respectively, based on the recommendations for the heat treatment of high-speed steels.[27,28] Martempering involved austenitization at 1150 °C for 2.5 min, followed by quenching at 510 °C for 10 min before air-cooling to room temperature. This quenching temperature was specifically chosen based on the CCT diagram, ensuring that transformation to pearlite was avoided while reducing thermal stresses before complete martensitic transformation. Austempering followed a similar quenching process to 510 °C, but the samples were then transferred to a 235 °C salt bath. The austempering duration was set at 72 h to maximize bainitic transformation, as the kinetics of bainite formation at lower temperatures are significantly slower.[29] This temperature was chosen based on the TTT diagram, ensuring the formation of lower bainite, which provides superior fracture toughness compared to upper bainite due to finer carbide precipitation at the grain boundaries.[18]

All the specimens underwent a three-stage tempering process at 560 °C for 2 h to stabilize the microstructure and to reduce the retained austenite. The tempering temperature was selected based on the secondary hardening peak,[30] ensuring an optimal balance between hardness, toughness, and wear resistance.

Figure 2a and b present the heat-treatment cycles of martempering and austempering, respectively.

A labeling system was used to ensure consistent and unambiguous identification of the samples used in this study. Martempered and austempered specimens were labeled with the letters *M* and *A*, respectively, while the letter *T* was added after *M* or *A* for tempered samples. Thus, MT and AT denote martempered and austempered specimens after tempering, respectively.

Microstructural Characterizations

Metallographic preparation involved grinding with SiC papers up to 1200-grit, followed by polishing with 3-μm and 1-μm diamond pastes. For

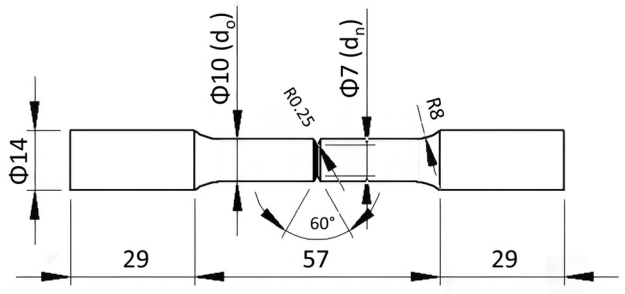

Fig. 1. Circumferential notch tensile × 0.3–40 × 0 specimen geometry (d_0 = 10 mm, d_n = 7 mm and turning tolerance = ± 0.1 mm).

Table I. Chemical composition of the samples used in the study (wt.%)

C	Si	Mn	P	S	Cr	Mo	Co	V	W	Ti	Al	Ni	Fe
1.13	0.52	0.30	0.02	0.01	3.62	5.44	8.01	2.70	6.72	0.01	0.03	0.10	Bal.

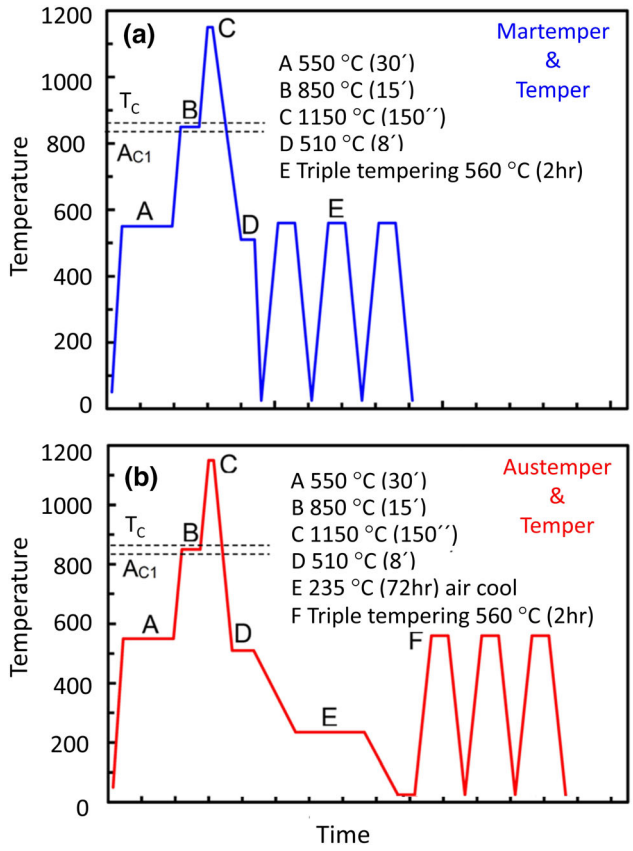

Fig. 2. Heat-treatment cycles for (a) martempering and (b) austempering processes.

electron backscatter diffraction (EBSD), the samples underwent additional polishing with colloidal silica for 3 h, followed by etching with Vilella's reagent for 40–60 s. Microstructural analysis was conducted using a Tescan Mira-3 field-emission scanning electron microscope (FE-SEM), and EBSD was performed on an FEI Quanta FEG 450 SEM equipped with an EBSD detector. Data were collected with a 30-nm step size over a 50 × 50 μm^2 area and analyzed using EDAX-TSL OIM Analysis™ software. EBSD identified alpha iron (α) as the BCC phase, while retained austenite, M_6C, and MC carbides were distinguished based on their crystal lattice parameters. A misorientation threshold of 5° with a 2-pixel resolution was used to define the grain boundaries. Martensitic/bainitic lath sizes were measured from EBSD maps using the linear intercept method (ASTM E112), averaging measurements in both vertical and horizontal directions. Prior austenite grain (PAG) reconstruction was performed using the Nishiyama–Wasserman method, which accurately reconstructs BCC-to-FCC orientation relationships using EBSD data. This method was chosen due to its high resolution and efficiency, despite potential limitations related to surface effects and data interpretation challenges.[31] To further validate this approach, back-scattered mode FE-SEM images were also used to visualize the PAG boundaries. Geometrically necessary dislocation (GND) density was calculated using Nye tensors derived from the EBSD orientation data. Kernel average misorientation (KAM) maps, ranging from 0 to 5°, were generated to estimate local strain and stored energy. Phase analysis was conducted using a Bruker™ D8 Advance X-ray diffractometer (XRD) with Cu Kα radiation (40 kV, 30 mA). Data were collected over the 35–110° range (ASTM E975) with a 0.02° step size and a 2-s step time. Quantitative phase analysis was performed using the Rietveld method with HighScore Plus® 3.0 and Maud 2.55 (2015).

Mechanical Testing

Hardness measurements were performed using the Rockwell C method in accordance with ASTM E18. At least six measurements were taken per sample with a measurement error of ± 0.5 HRC. Tensile tests were conducted on three CNT specimens using an Instron™ 8502 testing machine at a crosshead speed of 1.0 mm/min. Fracture strength and toughness were calculated using Eqs.3[32] and 4,[33] respectively:

$$\sigma_f = F/\left(\pi d_n^2/4\right) \tag{3}$$

where σ_f stands for the fracture strength (MPa), d_n is the notch diameter (mm), and F is the load at fracture (N) obtained from the force–displacement curve.

$$K_C = 0.45\sigma_f d_0^{1/2} \tag{4}$$

where K_C is the fracture toughness (MPa $m^{1/2}$) and d_0 is the specimen diameter (m).

RESULTS AND DISCUSSION

Microstructural Observations and XRD Analysis

The SEM images of the M, A, MT, and AT samples are shown in Fig. 3a–f. The microstructure of the M sample (Fig. 3a) consists of austenite blokes (AB), martensite plates (MP), and undissolved carbides (UC), while the *A* sample (Fig. 3b) contains bainitic laths (BL), austenite blocks, and martensite plates. The transformation of austenite to martensite is restricted within small austenite blocks, and the martensitic transformation could not proceed further.[34,35] UC are observed in both microstructures, predominantly exhibiting a near-spherical morphology.

The tempering process did not significantly alter the overall microstructure at comparable magnifications. However, secondary carbides, which typically precipitate during tempering and range in size from about 2–20 nm,[36] become visible at higher magnifications, as shown in Fig. 3c and d for the MT and AT samples, respectively. Figure 3e and f shows

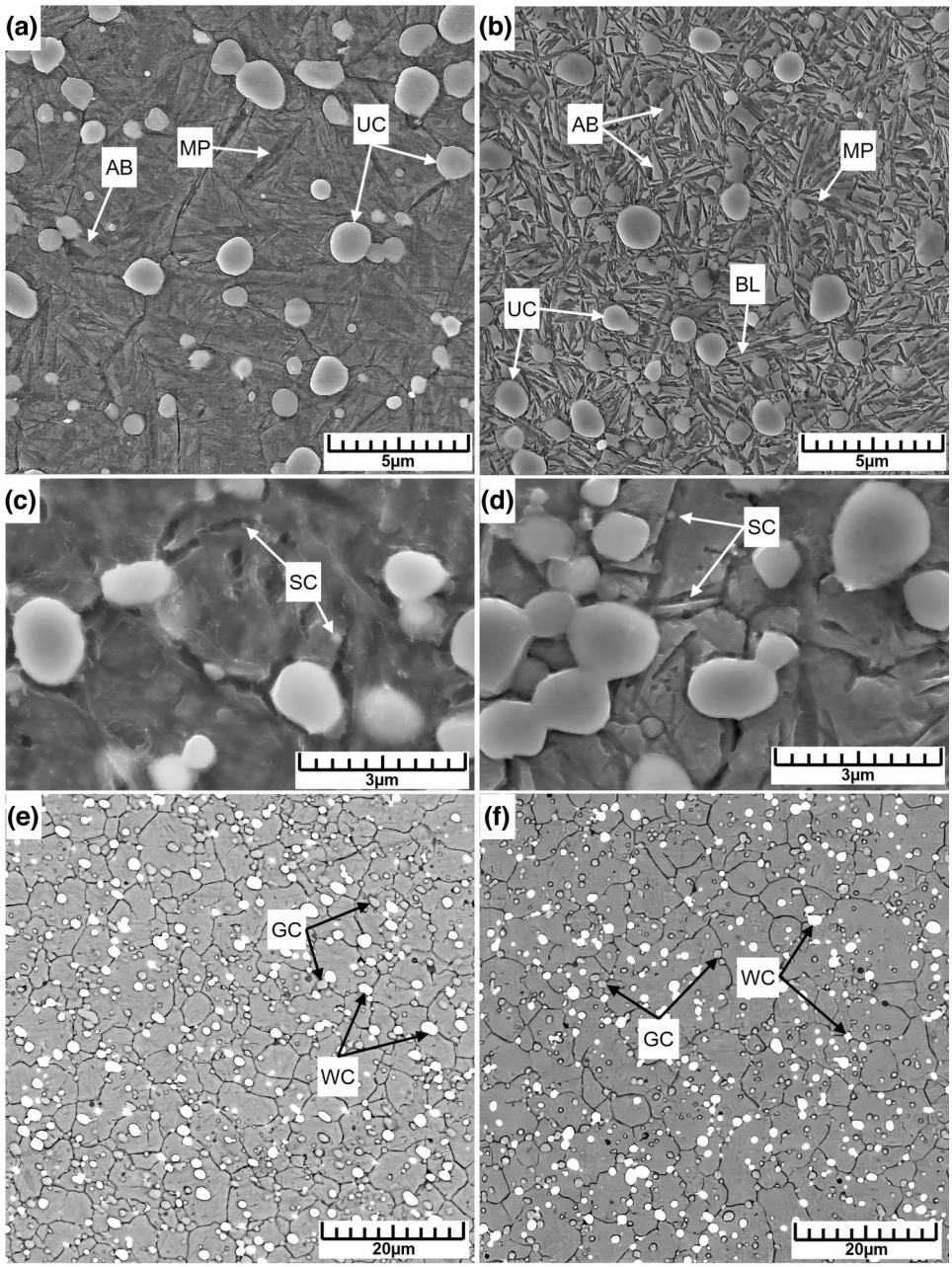

Fig. 3. SEM images of (a) martempered and (b) austempered samples. Images (c, e) correspond to martempered and tempered samples, while (d, f) show austempered and tempered samples. Arrows indicate undissolved carbides (UC), austenite blocks (AB), martensite plates (MP), bainitic laths (BL), secondary carbides (SC), white carbides (WC), and gray carbides (GC). Primary austenite grain (PAG) boundaries are also visible in (e) and (f), captured in backscattered imaging mode.

SEM images of the MT and AT samples captured using EBSD, highlighting the carbides in two contrasting colors, white and gray, corresponding to their compositional differences. Energy-dispersive spectroscopy (EDS) microanalysis (summarized in Table II) indicated that the white carbides are rich in molybdenum and tungsten, while the gray carbides are rich in vanadium. These findings align with previous reports, which indicate that M_6C-type carbides typically appear bright and spherical,

Table II. Chemical composition (wt.%) of the white and gray carbides and the matrix in the M sample, as shown in Fig. 3f

	V	Cr	Mo	W	Co	Fe
UC (gray)	20.4	5.40	9.40	8.00	8.50	48.30
UC (white)	2.94	4.35	24.54	38.31	3.36	26.50
Matrix	1.14	4.27	4.08	3.48	9.18	77.85

being rich in W and Fe, while gray carbides are either MC-type (enriched in V) or M_7C_2 and $M_{22}C_6$ types, which are rich in C.[37–41]

Table III shows that the surface fraction of the identified carbides in the MT microstructure is marginally higher than that in the AT sample. Furthermore, the mean diameter of the UCs in the MT sample is smaller than in the AT sample. According to the table, the lower volume fraction of undissolved carbides in the austempered samples compared to the martempered ones is due to the precipitation of nanocarbides during the austempering stage, which cannot be detected by SEM at high magnification.

Figure 4 shows the XRD patterns of the MT and AT samples. The identified phases include ferrite (α), austenite (γ), and several types of carbides, namely Co_3W_3C, Fe_6W_6C, and VC, corresponding to the M_6C, $M_{12}C$, and MC classifications, respectively. All of these carbides crystallize in a face-centered cubic (FCC) structure (Table IV).

Lattice strain causes a shift in the position of XRD peaks and their broadening.[42] Equation 5[43] is used to determine the extent of this strain:

$$\varepsilon = \frac{\beta_{hkl}}{4\tan\theta} \tag{5}$$

where ε is the lattice strain, β_{hkl} is the full width at half-maximum (FWHM) of the hkl planes, and θ is the Bragg angle.

The calculated microstrain values for the ferrite phase from the (110) and (211) peaks are listed in Table V. The average microstrain values ($\bar{\varepsilon}$) were calculated and the dislocation density (ρ_{SSD}) was determined using Eq. 6.[44] Both $\bar{\varepsilon}$ and ρ are provided in Table V.

Table III. Surface area fraction (f_c) and mean diameter size (D_c) of undissolved carbides (UC) in the as-quenched and austempered samples, measured via SEM images

Sample	D_c (μm)	f_c (%)
MT	0.76 ± 0.05	18.2 ± 0.7
AT	0.82 ± 0.05	15.2 ± 0.5

Table IV. Volume fractions of ferrite (α), austenite (γ), and carbides of nano and undissolved M_6C + $M_{12}C$ + MC determined using XRD

Specimen	α (%)	γ (%)	M_6C + $M_{12}C$ + MC (%)
AT	63	2	35
MT	62	5	33

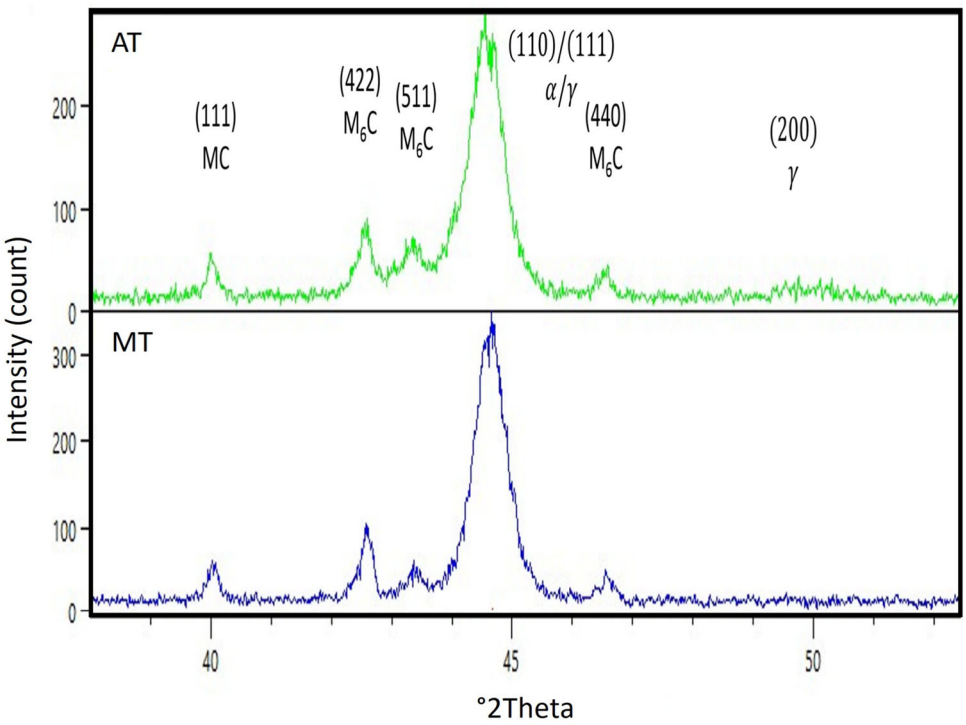

Fig. 4. X-ray diffraction (XRD) patterns of the martempered (MT) and austempered (AT) samples. The identified phases include ferrite (α), austenite (γ), and carbide phases such as Co_3W_3C, Fe_6W_6C, and VC, corresponding to the M_6C, $M_{12}C$, and MC types, respectively. Peak positions and intensities reflect differences in phase composition and lattice strain among the samples.

Table V. $2\theta^{\circ}$ and FWHM, calculated microstrain, and dislocation density (ρ) of the martempered and austempered specimens after tempering

Specimen	Plane	$2\theta^{\circ}$	FWHM (rad)	ε(%)	$\bar{\varepsilon}$(%)	$\rho \times 10^{14}$ (m^{-2})
MT	(110)	44.505	0.0159	0.969	0.92	20.1
	(211)	81.958	0.0299	0.861		
AT	(110)	44.462	0.0141	0.864	0.91	19.8
	(211)	81.837	0.0330	0.953		

$$\rho_{SSD} = \frac{1.44\bar{\varepsilon}^2}{b^2} \quad (6)$$

where $\bar{\varepsilon} = (\sum_{i=0}^{n} \varepsilon^2/n)^{\frac{1}{2}}$ is the average microstrain,[45] b is the Burgers vector (0.254 nm for BCC phase), and n is the number of hkl planes analyzed.

Table V shows that the calculated dislocation density values for the AT and MT samples are not significantly different.

The mean PAG sizes for the *M* and *A* samples were determined using the intercept method, as described in ASTM E112 standard, and are listed in Table IV. It is evident that the PAG sizes for both samples are nearly identical. Since the primary austenite grain size in steels is mainly influenced by the austenitizing temperature, this observation is consistent with expectations.

EBSD Analysis

Figure 5a and c (MT sample) and 5b and d (AT sample) show the EBSD phase maps of the martempered and austempered specimens, respectively. The microstructures of both samples primarily consist of body-centered cubic (BCC) ferrite/martensite (shown in red) and FCC phases (shown in green), which include MC/M_6C-type carbides and, to a lesser extent, retained austenite. The green regions are predominantly attributed to carbides, with minor contributions from retained austenite. The black areas observed in the EBSD maps likely correspond to regions where carbides were mechanically detached during sample preparation. These detached regions are more frequently observed in the martempered sample (Fig. 5a), particularly adjacent to carbides. Since both specimens underwent identical metallographic preparation and originated from the same base material, and considering that the austempered matrix is tougher, such detachment regions are less prominent in the AT sample (Fig. 5b). Additionally, extremely fine-scale secondary carbides (SC) are visible at higher magnification in the austempered sample (Fig. 5d), indicating a more refined microstructural evolution in this condition.

Table VII presents the area fractions and average size of the FCC phase, as determined from EBSD micrographs for both the martempered (MT) and austempered (AT) samples. While the FCC phase fraction remains constant at 17% in both samples, a slight increase in the average diameter is observed in the AT sample (from 0.98 μm to 1.01 μm). However, this difference is negligible and falls within the range of overlapping standard deviations (SD = 0.45 for MT and SD = 0.57 for AT), indicating that no significant coarsening occurred during the prolonged austempering stage.

Table VI. Maximum inscribed circle (MIC) and maximum circumscribed circle (MCC) diameters within and outside the primary austenite grains (PAG), along with the mean PAG diameter

Sample	MIC (μm)	MCC (μm)	PAG (μm)
M	2.59 ± 0. 5	9.6 ± 2	6.10 ± 1
A	2.92 ± 0. 4	9.3 ± 2	6.11 ± 1

The observed discrepancy between the FCC (carbide + austenite) volume fractions reported in Table IV (XRD) and Table VII (EBSD) stems from fundamental differences in the detection principles, resolution, and phase identification capabilities of the two techniques. XRD quantifies all the crystalline phases present within the sampling depth, including nanometer-scale carbides (2–30 nm) that commonly precipitate during tempering of tool steels. Because XRD averages signals over a large volume and can detect coherent diffraction from even very fine particles, providing a total volume fraction of all FCC-based phases, regardless of their size.

In contrast, EBSD is limited by its spatial resolution and can only resolve phases larger than ~ 30 nm, due to the need for well-defined Kikuchi patterns for accurate indexing.[46] Consequently, nanoparticles below this size threshold cannot be reliably identified and are excluded from EBSD-based quantification. Therefore, the FCC phase fraction in Table VII only accounts for coarser particles, resulting in a lower measured volume fraction compared to XRD. This limitation has been observed in similar studies. For example, Moshtaghi et al.[47] reported discrepancies between martensite phase fractions measured by XRD and by EBSD. This behavior parallels the challenges encountered here in carbide phase quantification, confirming that EBSD underestimates fine phases while XRD captures them more comprehensively. In Table VII, "Low confidence index points" refer to regions where

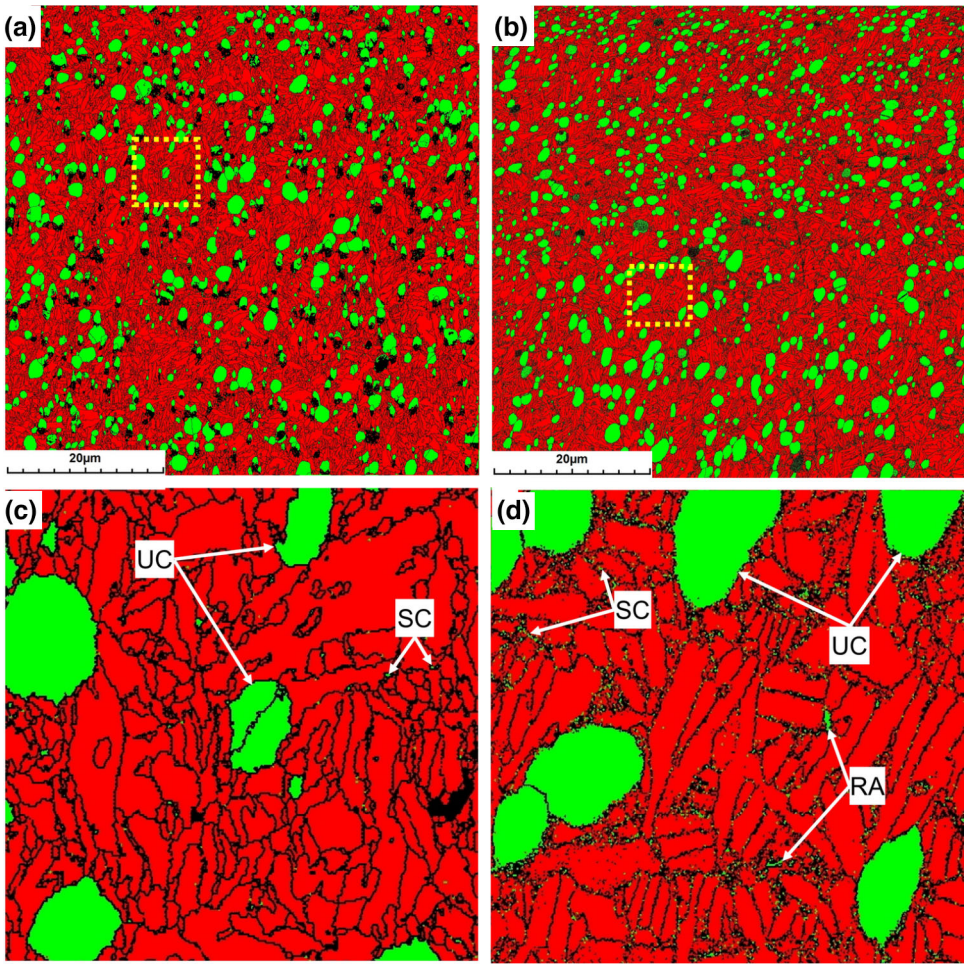

Fig. 5. EBSD phase and boundary maps (CI > 0.1) of (a, c) martempered (MT) and (b, d) austempered (AT) samples. The FCC phases—including undissolved carbides (UC), secondary carbides (SC), and retained austenite (RA)—are shown in green, while BCC ferritic phases are displayed in red. Maps (a) and (b) show broader views of the microstructure, whereas (c) and (d) present higher magnifications, highlighting fine details such as the morphology and distribution of *RA* and carbides.

Table VII. Area fractions (%) of FCC and BCC phases, low confidence index points, and average FCC phase size (μm), determined by EBSD analysis for martempered and austempered samples after tempering

Specimen	FCC (%)	BCC (%)	Low confidence index points (%)	FCC average diameter (μm)
MT	17	76	7	0.98 (SD = 0.45)
AT	17	64	19	1.01 (SD = 0.57)

the confidence index (CI) falls below a typical threshold value (< 0.1). These points are predominantly associated with nanometer-sized carbides and fine-scale porosities, which are inherent to the powder metallurgy process. Due to their extremely small size (typically < 30 nm), such nanocarbides do not generate distinct Kikuchi patterns and cannot be reliably indexed by EBSD. As a result, they are excluded from phase fraction quantification and appear as black regions in Fig. 5. To extract a more accurate fraction of nanocarbides larger than

Table VIII.. Prior Austenite Grain (PAG) size, bainitic ferrite lath size and geometrically necessary dislocations (GNDs) in martempered and austempered samples as determined from EBSD analyses

Sample	PAGs (μm)	Lath size (μm)
MT	5.79 (SD = 2.92)	0.25 (SD = 0.20)
AT	5.01 (SD = 2.98)	0.24 (SD = 0.19)

30 nm, FCC-phase inverse pole figure (IPF) maps were used. Reconstructed PAG maps for the AT sample were generated using a model based on the Nishiyama–Wasserman relationship between parent and daughter phases. The corresponding PAG sizes for both samples are presented in Table VIII. Notably, the difference between the PAG size and the prior austenite grain size ($D_{mean} \sim 6\ \mu m$), calculated before tempering (Table IV), is minimal for both cases. This suggests that the triple tempering process at sub-A_{c1} temperatures had a limited effect on PAG size.

For boundary classification, misorientation angles below 15° are categorized as low-angle boundaries (LAB), while those between 15° and 62° are considered high-angle boundaries (HAB).[48] Figure 6 shows the boundary maps with two misorientation ranges, 2–15° and 15–62°, for the MT and AT samples.

Mechanical Properties

The load–displacement diagram of the CNT tests for the MT and AT specimens is shown in Fig. 7, and the corresponding fracture strength and fracture toughness and the Rockwell C hardness values are listed in Table IX. The results show that the fracture strength and fracture toughness of the AT sample exceeds those of the MT sample.

Gomes et al.[49] have shown a correlation between yield strength and fracture toughness in high-speed steels. The relationship between the yield strength of steels and measurable microstructural features can be described by:[50]

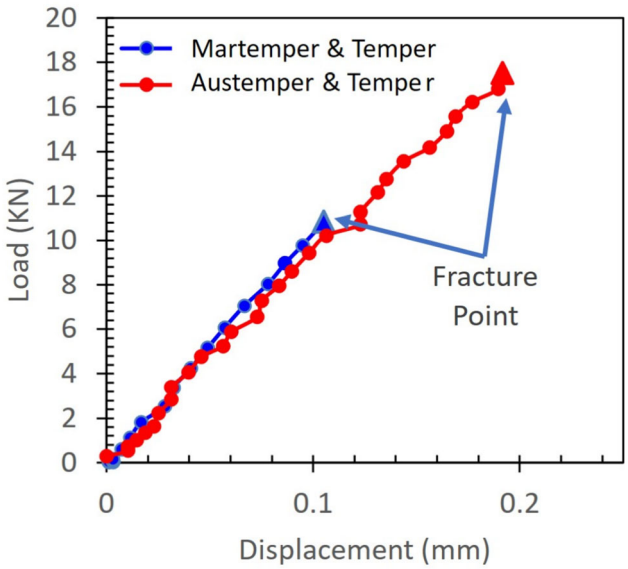

Fig. 7. Load–displacement diagram of the CNT test for MT and AT samples.

Table IX. Fracture strength, fracture toughness, and hardness of MT and AT samples

Specimen	σ_f (MPa)	Kc (MPa $m^{1/2}$)	Hardness (HRC)
MT	288 ± 18	10.9 ± 1.0	65.0 ± 0.2
AT	442 ± 28	17.0 ± 1.5	65.1 ± 0.5

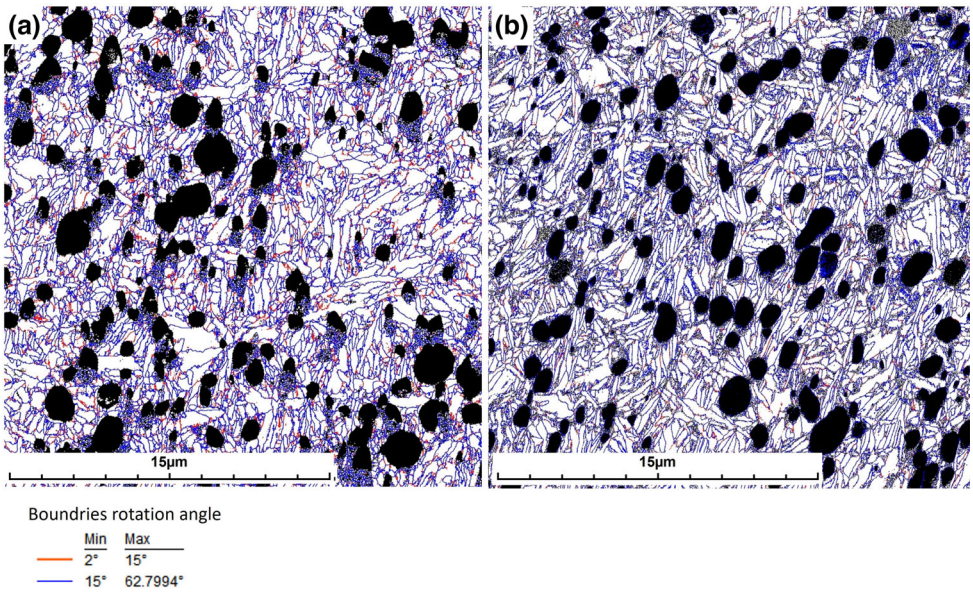

Fig. 6. Boundary maps with misorientation angles ranging from 2° to 62° of (a) MT and (b) AT samples.

$$\sigma_T = \left(\left(\sigma_{ss} + \sigma_Y + \sigma_P\right)^2 + {\sigma_d}^2\right)^{1/2} \quad (7)$$

where σ_T is the yield strength, σ_Y is the grain size contribution, σ_p, is the precipitation contribution, σ_{ss} is the solid-solution contribution, and σ_d is the dislocation contribution.

In the present study, as the austenitizing temperature was the same for both samples, it is presumed that σ_{ss} is identical for both martempered and austempered conditions. The grain size or lath width and dislocations density contributions can be estimated using Eqs. 8 and 9, respectively.[51–53]

$$\sigma_Y = K_{HP} d^{-\frac{1}{2}} \quad (8)$$

$$\sigma_d = \alpha M G b \rho^{\frac{1}{2}} \quad (9)$$

where d is the grain diameter or ferrite lath width, M is the Taylor factor (2.73 for the BCC phase), G is the shear modulus (82 GPa), b is the Burger's vector, ρ is the average density dislocation density, and K_{HP} (0.21 MPa $m^{-1/2}$) and α (0.25) are constants.

To compare the parameters of Eq. 7 for the martempered and austempered samples, the dislocation density (ρ_{SSD}), PAGs, and ferrite plate sizes were determined and are listed in Tables V and VIII. These data indicate that the primary austenite grains and ferrite laths in the austempered sample are slightly smaller than those in the martempered sample, while the dislocation density is nearly identical in both microstructures. Consequently, it can be conclude that the influence of grain size, ferrite lath length, and dislocation contribution (from Eq. 9) on the improved fracture strength of the AT specimen is relatively minor.

The dominant strengthening mechanism in polycrystalline materials reinforced with non-shearable dispersoids is the Orowan mechanism. When dislocations encounter fine, hard particles that cannot be sheared, they bow around them, forming Orowan loops. This increase dislocation storage and enhance strain hardening. This behavior has been widely reported in materials with incoherent dispersoids, such as Cr-containing alloys.[54] Given that the dispersoids in our study exhibit similar characteristics, the Orowan equation (Eq. 10)[55] is appropriate for describing their strengthening contribution:

$$\sigma_P = \left(\frac{0.538 G b f^{\frac{1}{2}}}{D}\right) Ln\left(\frac{D}{2b}\right) \quad (10)$$

where G is the shear modulus, b is the Burgers vector (0.248 nm), f is the volume fraction of hard particles, and D is the diameter of the particles.

According to Eq. 10, the precipitated carbides significantly influence dislocation motion and matrix strengthening. Table III shows that the surface fraction of identified UC in the MT sample is marginally higher than in the AT sample. Furthermore, the mean diameter of UC in the MT sample is smaller. This apparent discrepancy of the lower carbide fraction in AT results from the inability of SEM imaging at high magnification to detect nanoscale carbides formed during the austempering stage.

Based on Eq. 10, the calculated strengthening contribution from undissolved carbides (σ_P^{UC}), derived using the volume fractions and average diameters from the FESEM images (Table X), indicates that the contribution is slightly greater in the AT sample than in the MT sample. The IPF maps for MT and AT samples are shown in Fig. 8a and d, while Fig. 8b and e present magnified views highlighting fine carbides (FC) and untransformed carbides (UC), marked by arrows. The austempered sample clearly exhibits a higher area fraction of FCs, particularly within the ferrite laths. Wen et al.[56] studied the precipitation kinetics of $M_{23}C_6$ carbides in heat-resistant steels with fine-grained microstructures, observing that fine and coarse $M_{23}C_6$ carbides form at both low-angle grain boundaries (LAGBs) and HAGBs. Similarly, Qi et al.[57] reported that the addition of Cr–Mo increases the number and density of fine carbides, thereby improving the steel's strength. Haj Slama et al.[58] also observed fine carbide precipitation as separated films at HAGBs after austempering Fe5Ni0.13C steel for 5 h. In line with Ohmori et al.,[59] the higher FC content in the AT sample may be attributed to faster carbon diffusion during bainitic transformation compared to martensite formation, leading to carbide formation at ferrite–cementite interfaces.

Fine carbides, visible in the IPF maps (Fig. 8b and e), range in size from 30 to 60 nm. Their area fractions, listed in Table X, are 1.7% for the MT sample and 11% for the AT sample. According to Eq. 10, the strengthening contribution from these fine carbides (σ_P^{FC}) is significantly higher for the AT sample due to its larger volume fraction.

The formation of fine carbides in austempered steels is closely related to bainitic transformation, especially the formation of lower bainite at temperatures between 200 and 300 °C.[60,61] During austempering, bainitic ferrite forms via a diffusionless mechanism, followed by carbon partitioning into the surrounding austenite. Due to the low solubility of carbon in bainitic ferrite, excess carbon precipitates as nanocarbides within laths and along interfaces. These fine carbides hinder dislocation motion, enhancing strength. In silicon-containing steels, carbide precipitation is delayed, allowing for carbon enrichment and stabilization of adjacent austenite.[62,63]

In high-speed steels like PM ASP2030, the B/M duplex microstructure formed via austempering and tempering provides advantages over fully martensitic structures. Specifically, tempering at 550 °C facilitates nanoscale secondary carbide precipitation from the retained austenite. Wang et al.[18]

Table X. Contribution of measured microstructural characteristics on strengthening and increasing fracture toughness

Specimen	LAGB (2–15)° (μm^{-1})	HAGB (15–62)° (μm^{-1})	KAM (°)	ρ_{GND} ($\times 10^{14}$ m^{-2})	σ_P^{UC} (MPa)	σ_P^{FC} (MPa)	σ_d (MPa)
MT	1.96	7.48	0.67°	4.6	44.7	514.4	1210
AT	1.75	23.68	1.18°	8.1	38.3	785.8	1590

reported similar behavior in B/M structures, which resulted in more uniform and finer carbide dispersion compared to coarser carbides in fully martensitic microstructures, thereby improving both strength and toughness.[64] KAM, derived from local lattice curvatures, measures local plastic strain and dislocation density in deformed microstructures.[65,66] Figure 9 shows that KAM values are higher at the boundaries of martensitic/bainitic ferrite laths than at their cores, suggesting localized strain at lath interfaces. Notably, the AT sample exhibits a significantly higher average KAM (1.18°) than the MT sample (0.67°), indicating a greater density of GNDs and thus higher stored internal energy. The GND density (ρ_{GND}) was calculated using Eq. 11, which correlates KAM with dislocation density:[67]

$$\rho_{GND} = \frac{\alpha < \theta >}{bd} \tag{11}$$

where $\alpha = 3$ is a constant for tilt dislocations, θ is the KAM value (in radians), b is the Burgers vector, and d is the EBSD step size.

GNDs, which accommodate lattice curvature from strain gradients, play a critical role in hardening and energy absorption, while statistically stored dislocations (SSDs) result from random entanglements. SSD density was derived from the XRD data using Eq. 6, with the results summarized in Table V. Although SSDs are generally more numerous, GNDs have a more pronounced impact due to their directional and localized nature as reported in a previous study.[67]

As listed in Table X, the AT sample shows a significantly higher ρ_{GND} (8.1×10^{14} m^{-2}) compared to the MT sample (4.6×10^{14} m^{-2}). This increase in GND density enhances dislocation resistance and improves energy absorption capacity, directly contributing to the higher fracture toughness in the AT sample. Other EBSD-derived features also contribute. The (HAGB density is significantly greater in the AT sample (23.68 μm^{-1} versus 7.48 μm^{-1} in MT), aiding crack deflection and energy dissipation. Although the MT sample has slightly higher LAGB density (1.96 μm^{-1} versus 1.75 μm^{-1} in AT), their lower misorientation makes them less effective in hindering dislocation motion. Together, the elevated KAM values, higher GND and HAGB densities, and greater strengthening from fine carbides explain the superior fracture toughness of the AT sample. These findings align with those of Moshtaghi et al.,[67] who demonstrated a link between GND accumulation, HAGB density, and enhanced dislocation storage.

In practical terms, the higher KAM in the AT sample reflects its improved ability to accommodate strain gradients and store deformation energy without premature failure, enhancing not only strength and toughness but also performance under cyclic or impact loads, key attributes in high-speed tool steels.

While the present study offers a comprehensive analysis of the microstructural and mechanical differences between martempered and austempered PM ASP2030 steel, further investigations could provide deeper insight into the underlying mechanisms. The current characterization primarily relied on SEM, EBSD, and XRD techniques, which effectively captured features such as dislocation density, grain boundary characteristics, and carbide distribution. However, advanced characterization methods, such as transmission electron microscopy or 3D tomography, may help reveal nanoscale features, particularly the morphology and dispersion of precipitated carbides and the substructure of dislocation arrays, which remain unresolved at the current scale.

From a mechanical perspective, the scope of this study focused on hardness and fracture toughness as the primary indicators of performance. Additional evaluation of tensile strength, fatigue resistance, and wear behavior under various loading regimes could complement the current findings and provide a more holistic understanding of the performance benefits of austempered versus martempered microstructures in real-world applications. These aspects merit further attention in future investigations aimed at optimizing heat-treatment strategies for high-performance tool steels. Considering the improved fracture toughness and refined microstructure achieved through austempering, potential industrial applications may include blanking, broaching, cold forging, cold work, cutting tools, drills, fine blanking, knives, plastic injection molds, powder compaction, reamers, rolls for rolling mills, and taps.[28]

CONCLUSION

This study revealed distinct microstructural differences between martempered (MT) and austempered (AT) PM ASP2030 steel after tempering.

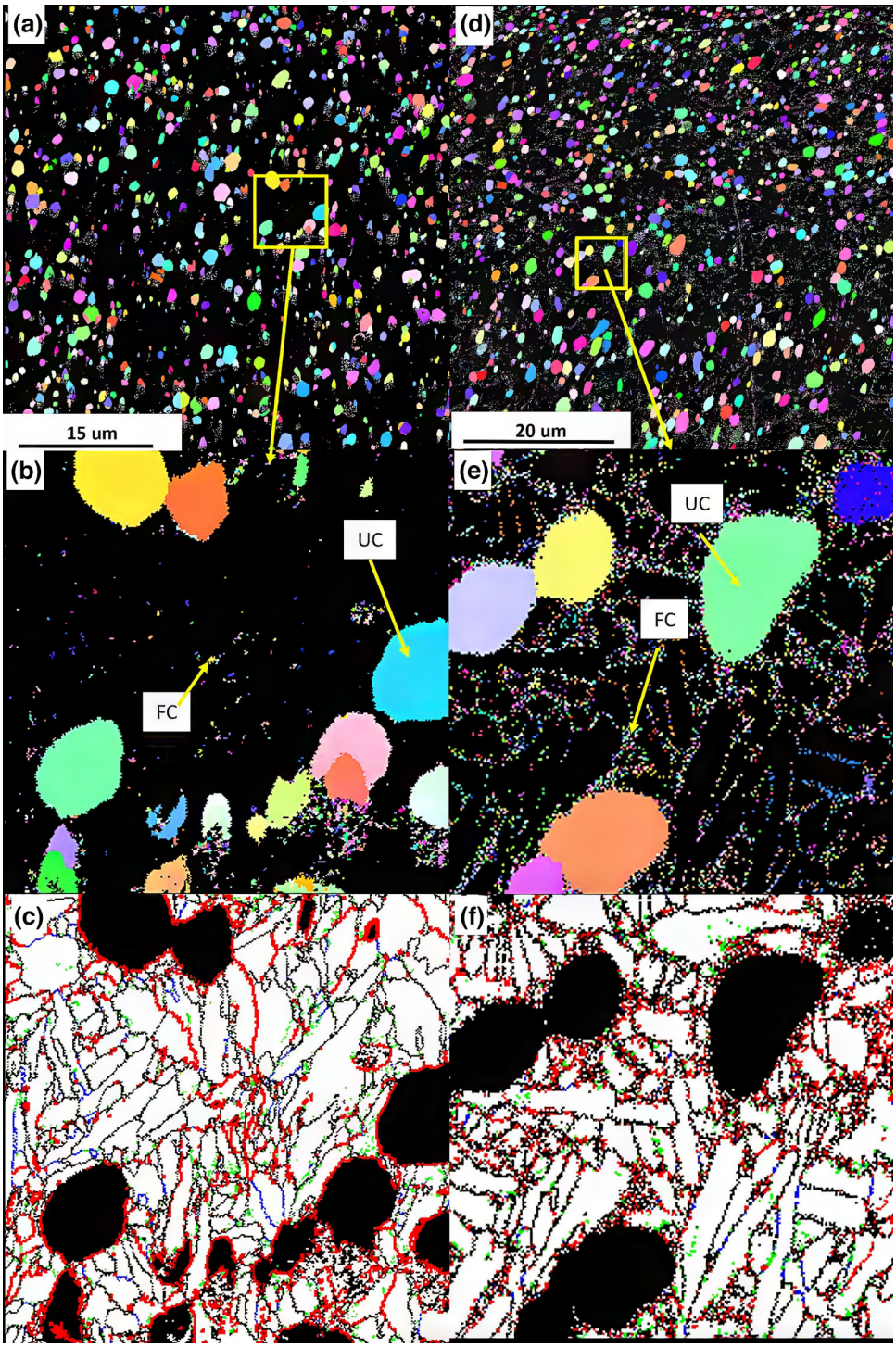

Fig. 8. (a, d) Inverse pole figure (IPF) maps of martempered (MT) and austempered (AT) samples, respectively. (b, e) Magnified views highlighting the distribution of fine carbides (FC) and untransformed carbides (UC), indicated by arrows. The austempered sample (e) exhibits a higher area fraction of fine carbides within the ferrite laths compared to the martempered sample (b). (c, f) Corresponding boundary maps for (b) and (e), illustrating grain and phase boundaries. The increased presence of fine carbides in the austempered sample (f) is evident, contributing to its microstructural refinement.

While both samples exhibited similar phases, grain sizes, and overall dislocation densities, the AT sample showed a significantly higher fraction and total length of high-angle grain boundaries, a greater kernel average misorientation (KAM), and a larger volume of nano-sized carbides. Despite comparable hardness values, the AT sample demonstrated substantially higher fracture toughness than the MT sample. This improvement is attributed to the combined effects of its refined

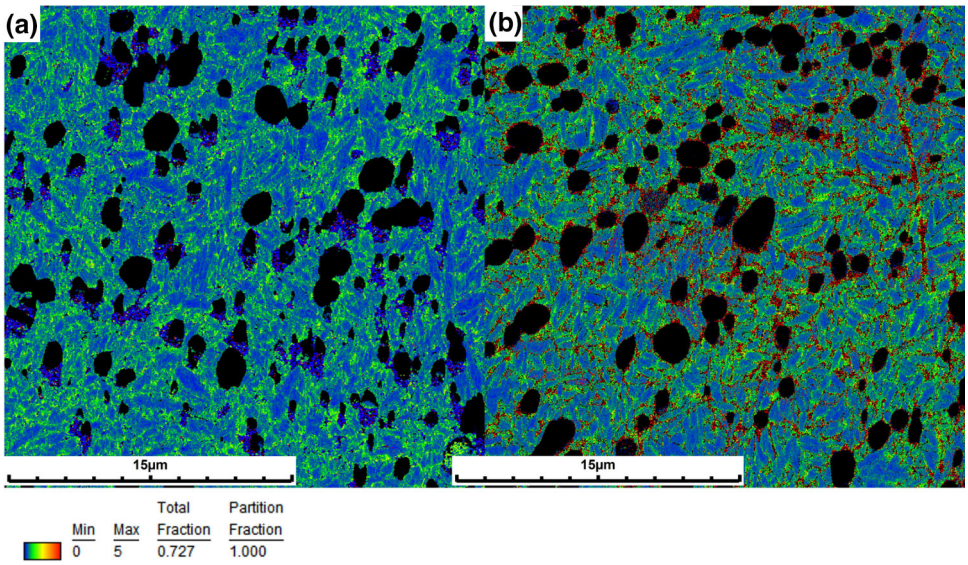

Fig. 9. KAM maps of (a) MT and (b) AT samples.

microstructure, specifically, the increased density of high-angle grain boundaries that impede crack propagation, the elevated KAM indicating enhanced strain accommodation, and the more pronounced strengthening from the higher volume of fine carbides that hinder dislocation motion.

These findings underscore the critical role of the austempering heat treatment in tailoring the microstructure of PM ASP2030 steel to achieve superior fracture toughness, a key property for high-performance tooling applications.

CONFLICT OF INTEREST

On behalf of all authors, the corresponding author states that there is no conflict of interest.

REFERENCES

1. Y. Luo, H. Guo, X. Sun, M. Mao, and J. Guo, *Metals* 7, 27 https://doi.org/10.3390/met7010027 (2017).
2. T.V. Alan M. Bayer and Bruce A. Becherer, *ASM Handbook*, (1989), pp 51.
3. R.A. Mesquita, C.A. Barbosa, C.S. Gonçalves, and A.L. Slaviero, *Int. Heat Treat. Surf. Eng.* 5, 36 https://doi.org/10.1179/174951411X12956208225221 (2011).
4. V.L. Franjo Cajner, Dragan Pustaić, *Key Eng. Mater.*, 592 (2014). https://doi.org/10.4028/www.scientific.net/KEM.592-593.680.
5. S. Solic, Z. Schauperl, M. Godec, and V. Troqaa, *Tehnički Glasnik* 11, 121 (2017).
6. B.A. Behrens, and F. Schäfer, *Steel Res. Int.* 80, 887 https://doi.org/10.2374/SRI09SP143 (2009).
7. J.Y. Liu, A.H. Li, J.C. Zhang, Y.Q. Wang, and Z.H. Feng, *Exp. Tech.* 47, 395 https://doi.org/10.1007/s40799-022-00560-x (2023).
8. Z. Yang, Z. Liu, X. He, S. Qiao, and C. Xie, *Sci. Rep.* 8, 1 https://doi.org/10.1038/s41598-017-18434-3 (2018).
9. K. Wang, F. Hu, W. Zhou, D. Zhang, C. Yin, S. Yershov, and K. Wu, *J. Mater. Res. Technol.* 26, 5773 https://doi.org/10.1016/j.jmrt.2023.09.003 (2023).
10. N. Zhang, G. Zhu, B. Dai, Y. Zhao, Z. Wang, B. Jiang, Y. Liu, and C. Wu, *Mater. Sci. Eng. A* 901, 146515 https://doi.org/10.1016/j.msea.2024.146515 (2024).
11. B. Avishan, S. Yazdani and S. Hossein Nedjad, *Mater. Sci. Eng. A*, 548 (2012). https://doi.org/10.1016/j.msea.2012.03.098.
12. M.N. Yoozbashi, R. Zolfaghari, S. Yazdani, and S. Tekeli, *J. Mater. Eng. Perform.* https://doi.org/10.1007/s11665-023-08971-6 (2024).
13. A. Firouzi, S. Yazdani, R. Tavangar, B. Shakerifard and F. Khan Md, *Strength Mater.* 54, 1064 (2022). https://doi.org/10.1007/s11223-023-00482-y.
14. A. Firouzi, S. Yazdani, R. Tavangar, B. Shakerifard, and F.K. Mohammad, *Metall. Res. & Technol.* 119, 211 https://doi.org/10.1051/metal/2022025 (2022).
15. S. Golchin, B. Avishan, and S. Yazdani, *Mater. Sci. Eng. A* 656, 94 https://doi.org/10.1016/j.msea.2016.01.025 (2016).
16. Z.-J. Luo, J.-C. Shen, H. Su, Y.-H. Ding, C.-F. Yang, and X. Zhu, *J. Iron Steel Res. Int.* 17, 40 https://doi.org/10.1016/S1006-706X(10)60168-9 (2010).
17. J. Chakraborty, P.P. Chattopadhyay, D. Bhattacharjee, and I. Manna, *Metall. Mater. Trans. A* 41, 2871 https://doi.org/10.1007/s11661-010-0288-1 (2010).
18. F. Wang, D. Qian, H. Mao, Y. He, and B. Shu, *J. Mater. Res. Technol.* 9, 6712 https://doi.org/10.1016/j.jmrt.2020.04.075 (2020).
19. F.G. Caballero, H. Roelofs, S. Hasler, C. Capdevila, J. Chao, J. Cornide, and C. Garcia-Mateo, *Mater. Sci. Technol.* 28, 95 https://doi.org/10.1179/1743284710Y.0000000047 (2012).
20. L. Qian, Q. Zhou, F. Zhang, J. Meng, M. Zhang, and Y. Tian, *Mater. Des.* 39, 264 https://doi.org/10.1016/j.matdes.2012.02.053 (2012).
21. L.C. Chang, *Mater. Sci. Eng. A* 368, 175 https://doi.org/10.1016/j.msea.2003.10.297 (2004).
22. P. Huyghe, M. Caruso, J.L. Collet, S. Dépinoy, and S. Godet, *Metall Mat Trans A Phys Metall Mat Sci* 50, 3486 https://doi.org/10.1007/s11661-019-05281-2 (2019).
23. K.S. Kumar, A. Lawley, and M.J. Koczak, *Metall. Trans. A* 22, 2733 https://doi.org/10.1007/bf02851368 (1991).
24. Z. Zhao, C. Liu, Y. Liu, and D.O. Northwood, *J. Mater. Sci.* 36, 5045 https://doi.org/10.1023/A:1011874708194 (2001).
25. D. Candane, A. Natarajan, and K. Palaniradja, *Int. J. Mater. Sci. Appl.* 2, 56 https://doi.org/10.11648/j.ijmsa.20130202.14 (2013).
26. S. Moritz, U. Ziesing, J. Boes, J. Lentz, S. Weber and M. Reuber, In *Procedia CIRP*, ed. M. Schmidt, F. Vollertsen and B.M. Colosimo (Elsevier B.V.: 2022), pp 171.
27. G.K. George Roberts, Richard Kennedy, *High speed steels*, (American Society for Materials, USA, 1998).

28. Erasteel, "ASP2030", https://www.erasteel.com/products/asp2030/.
29. Z. Zhang, F. Shi, L. Yin, Q. Pang, W. Leng, and L. Xu, *Jinshu Rechuli* 48, 87 https://doi.org/10.13251/j.issn.0254-6051.2023.08.014 (2023).
30. D.R. Johnson, and W.T. Becker, *J. Mater. Eng. Perform.* 2, 255 https://doi.org/10.1007/BF02660294 (1993).
31. M. Moshtaghi, and M. Safyari, *Int. J. Hydrogen Energy* 48, 27408 https://doi.org/10.1016/j.ijhydene.2023.03.396 (2023).
32. J. Jin, R. Gao, H. Peng, H. Guo, S. Gong, and B. Chen, *Metall. Mater. Trans. A* 51, 2411 https://doi.org/10.1007/s11661-020-05661-z (2020).
33. K. Alaneme, *Mater. Res.* 14, 155 https://doi.org/10.1590/S1516 (2011).
34. J. Sun, T. Jiang, Y. Wang, S. Guo, and Y. Liu, *Mater. Sci. Eng. A* 726, 342 https://doi.org/10.1016/j.msea.2018.04.095 (2018).
35. J. Sun, F. Lian, Y. Sun, Y. Wang, S. Guo, and Y. Liu, *JOM* 75, 417 https://doi.org/10.1007/s11837-022-05582-9 (2023).
36. W. Rong, H.O. Andrén, H. Wisell, and G.L. Dunlop, *Acta Mater.* 40, 1727 https://doi.org/10.1016/0956-7151(92)90116-V (1992).
37. J. Zhang, X. Zhao, S. Li and L. Zhang, *Kang T'ieh*, 59 (2024). https://doi.org/10.13228/j.boyuan.issn0449-749x.20230307.
38. Z. Aringozhina, B. Rakhadilov, D. Yeskermessov, Y. Tabiyeva and W. Ahmed, *Innovations in materials chemistry, physics, and engineering research*, (IGI Global, 2023), pp 211.
39. Y.D. Koryagin and V.L. Il'ichev, In *Materials Science Forum*, (Trans Tech Publications Ltd: 2016), pp 558.
40. H.T. Cao, X.P. Dong, W.F. Li, Z. Pan, X.W. Wu, Q.W. Huang and J.J. Li, *Zhuzao*, 63 (2014).
41. M. Skakov, B. Rakhadilov, and G. Karipbayeva, *Appl. Mech. Mater.* 404, 20 (2013).
42. A.K.J. Mohammad Dani, Parikin, Andon Insani, Riza Iskandar, *Mal. J. Fund. Appl. Sci.*, 13 (2017).
43. M. Rabiei, A. Palevicius, A. Monshi, S. Nasiri, A. Vilkauskas, and G. Janusas, *Nanomater.* 10, 1627 https://doi.org/10.3390/nano10091627 (2020).
44. P.Y. Rajesh, K. Khatirkar, and S.G. Sapate, *ISIJ Int.* 52, 1370 https://doi.org/10.2355/isijinternational.52.1370 (2012).
45. K. Venkateswarlu, *Procedia Mater. Sci.* https://doi.org/10.1016/j.mspro.2014.07.260 (2014).
46. S.I. Wright, M.M. Nowell, R. De Kloe and L. Chan, In *microscopy and microanalysis*, (Cambridge University Press: 2014), pp 852.
47. M. Moshtaghi, and M. Safyari, *Steel Res. Int.* 92, 2000242 https://doi.org/10.1002/srin.202000242 (2021).
48. Z. Li, F. Chai, L. Yang, X. Luo, and C. Yang, *Mater. Des.* 191, 108637 https://doi.org/10.1016/j.matdes.2020.108637 (2020).
49. M.A. Gomes, C.S. Wright, and A.S. Wronski, *J. Mater. Sci.* 32, 1799 https://doi.org/10.1023/A:1018592404209 (1997).
50. V. Carretero Olalla, V. Bliznuk, N. Sanchez, P. Thibaux, L.A.I. Kestens, and R.H. Petrov, *Mater Sci. Eng. A* 604, 46 https://doi.org/10.1016/j.msea.2014.02.066 (2014).
51. M. Kabirmohammadi, S. Yazdani, A. Ghasemi, Z. Peng, T. Saeid, and M. Pouranvari, *Mater. Charact.* 216, 114291 https://doi.org/10.1016/j.matchar.2024.114291 (2024).
52. X. Xing, S. Huang, L. Li, J. Ouyang, J. Gao, S. Chen, and Z. Peng, *J. Mater. Res. Technol.* 25, 832 https://doi.org/10.1016/j.jmrt.2023.05.260 (2023).
53. H. Liu, P. Fu, H. Liu, and D. Li, *Mater.* 11, 583 https://doi.org/10.3390/ma11040583 (2018).
54. M. Safyari, M. Moshtaghi, T. Hojo, and E. Akiyama, *Corros. Sci.* 194, 109895 https://doi.org/10.1016/j.corsci.2021.109895 (2022).
55. Y. Wang, J. Sun, T. Jiang, Y. Sun, S. Guo, and Y. Liu, *Acta Mater.* 158, 247 https://doi.org/10.1016/j.actamat.2018.07.060 (2018).
56. P. Wen, Z. Chen, L. Yang, Z. Xie, D. Huang, Z. Liu, and H. Luo, *Metall. Mater. Trans. A: Phys.* 53, 4283 https://doi.org/10.1007/s11661-022-06823-x (2022).
57. M. Qi, H. Wu, L. Du, X. Gao, X. Zhang, Z. Zhang and M. Zhang, *Steel Res. Int.*, n/a (2023). https://doi.org/10.1002/srin.202300376.
58. M. Ben Haj Slama, N. Gey, L. Germain, J.C. Hell, K. Zhu, and S. Allain, *Metall Mater. Trans. A* 47, 15 https://doi.org/10.1007/s11661-015-3209-5 (2016).
59. Y. Ohmori, H. Ohtani, and T. Kunitake, *Met. Sci.* 8, 357 https://doi.org/10.1179/msc.1974.8.1.357 (1974).
60. B. Avishan, R. Karimkhani Shamloo, E. Akbarzadeh Chiniforoush, and S. Yazdani, *J. Mater. Eng. Perform.* 32, 4922 https://doi.org/10.1007/s11665-022-07446-4 (2023).
61. E.A. Chiniforush, S. Yazdani, M. Mohammadi, and N. Niki, *Int. J. Mater. Res.* 110, 106 https://doi.org/10.3139/146.111726 (2019).
62. H. Mousalou, S. Yazdani, N. Parvini Ahmadi, and B. Avishan, *Acta Metal Sin.* 33, 1635 https://doi.org/10.1007/s40195-020-01091-3 (2020).
63. B. Avishan, S. Mohammadzadeh Khoshkebari, and S. Yazdani, *Mater Chem Phys* 260, 124160 https://doi.org/10.1016/j.matchemphys.2020.124160 (2021).
64. D. Zheng, W. Zhao, X. Yu, Y. Su, and Y. Wei, *Steel Res. Int.* 96, 2400570 https://doi.org/10.1002/srin.202400570 (2025).
65. F.M. Carvalho, D. Centeno, G. Tressia, J.A. Avila, F.E.M. Cezario, A. Márquez-Rossy, E.A. Ariza, and M. Masoumi, *J. Mater. Res. Technol.* 18, 4590 https://doi.org/10.1016/j.jmrt.2022.04.066 (2022).
66. M. Kabirmohammadi, S. Yazdani, T. Saeid, and M. Pouranvari, *J. Mater. Res. Technol.* 33, 4033 https://doi.org/10.1016/j.jmrt.2024.10.092 (2024).
67. M. Moshtaghi, M. Safyari, S. Kuramoto, and T. Hojo, *Int. J. Hydrogen Energy* 46, 8585 https://doi.org/10.1016/j.ijhydene.2020.12.028 (2021).